Non-Equilibrium Carrier Transport in Strongly Coupled Quantum Dot Solids and Heterostructures

Mengxia Liu
University of Cambridge

Sachin Dev Verma
University of Cambridge

Zhilong Zhang
University of Cambridge

Jooyoung Sung
University of Cambridge

Akshay Rao (✉ ar525@cam.ac.uk)
University of Cambridge

Research Article

Non-Equilibrium Carrier Transport in Strongly Coupled Quantum Dot Solids and Heterostructures

Mengxia Liu,[1] Sachin Dev Verma,[1,2] Zhilong Zhang,[1] Jooyoung Sung,[1*] Akshay Rao[1*]

[1]*Cavendish Laboratory, University of Cambridge, JJ Thomson Avenue, Cambridge CB3 0HE, United Kingdom*

[2]*Department of Chemistry, Indian Institute of Science Education and Research Bhopal, Bhopal Bypass Road, Bhopal 462066, Madhya Pradesh, India*

*Correspondence and requests for materials should be addressed to Jooyoung Sung (Email: js2377@cam.ac.uk), or Akshay Rao (Email: ar525@cam.ac.uk)

13 **Understanding and controlling carrier dynamics in colloidal quantum dot (CQD) solids**

14 **is crucial for unlocking their full potential for optoelectronic applications. The recent**

15 **development of solution-processing methods to incorporate CQDs into high-mobility**

16 **semiconducting matrices opens new routes to control simultaneously electronic coupling**

17 **and packing uniformity in CQD solids. However, the fundamental nature of carrier**

18 **transport in such systems remains elusive. Here we report the direct visualisation of**

19 **carrier propagation in metal-halide exchanged PbS CQD solids and quantum-dot-in-**

20 **perovskite (QDiP) heterostructures via transient absorption microscopy. We reveal three**

21 **distinct transport regimes: an initial band-like transport persisting over hundreds of**

22 **femtoseconds, an Auger-assisted sub-diffusive transport before thermal equilibrium is**

23 **achieved, and a final hopping regime at longer times. The band-like transport was**

24 **observed to correlate strongly with the extent of carrier delocalisation and the degree of**

25 **energetic disorder. By tailoring the perovskite content in heterostructures, we obtained a**

26 **band-like transport length of 90 nm at room temperature and an equivalent diffusivity of**

27 **up to 106 cm^2 s^{-1} – which is four orders of magnitude higher than the steady-state values**

28 **obtained for PbS CQD solids. These findings not only shed light on the non-equilibrium**

29 **dynamics in CQD solids and their influence on carrier transport, but also introduce**

30 **promising strategies to harness non-equilibrium transport phenomena for more efficient**

31 **optoelectronic devices.**

32

33

34   Quantum dot and quantum well architectures, which exhibit tunable optical transitions

35   through the confinement of carriers at the nanoscale, are attractive building blocks for infrared

36   optoelectronics. They have been widely explored for photodetection and light emission. The

37   operation of these devices is fundamentally governed by the charge and exciton dynamics

38   within the active material. To achieve high performance metrics, high mobilities and minimised

39   trap state densities are necessary; this has thus far restricted the implementation of quantum

40   heterostructures to materials fabricated via high-temperature epitaxial methods.

41

42   The emergence of colloidal quantum dots (CQDs) – semiconductor nanocrystals that

43   benefit from solution processing at low temperatures – shows promise for the scalable

44   manufacturing of large-area devices, compatibility with flexible substrates, and standard

45   integrated circuits[1,2]. Rapid advances in materials processing have driven impressive

46   performance progress, but challenges remain to achieve full control over electronic properties.

47   Carrier mobilities in CQDs are typically low ($\sim 10^{-3}$–10^{-2} cm^2 V^{-1} s^{-1})[3]. Improved coupling

48   between individual CQDs - often through partial fusion - can increase the mobility by two to

49   three orders of magnitude (up to ~ 20 cm^2 V^{-1} s^{-1}), however, at the expense of discrete energy

50   levels[4,5]. Moreover, disorder and defects – consequences of low-temperature solution

51   processing – are inevitably present in CQD ensembles, in which their abundance results in an

52   inhomogeneous energy landscape and carrier losses[6,7]. It has been shown that coherent

53   transport is theoretically possible in epitaxially connected CQD arrays[8], while disorder,

54   including the size polydispersity of CQDs and the variation of inter-dot spacing, can lead to

55   localisation and elimination of delocalised states[9,10]. These intrinsic drawbacks in disordered

56   semiconductors affect the transport of excitons and charges and, therefore, limit device

57   performance.

58   A novel type of heterostructure, one that integrates colloidal nanocrystals epitaxially into

59   a perovskite matrix, offers an additional degree of freedom to control charge transport and

60   recombination for more efficient optoelectronic devices[11,12]. The quantum-dot-in-perovskite

61   (QDiP) materials take advantage of the compelling carrier transport properties of metal-halide

62   perovskites as well as the wide spectral tunability of quantum dots[13]. They exhibit electronic

63   and transport properties programmed at the nanoscale. By engineering the composition and

64   microscopic structure, QDiP materials can be tailored to deliver improved carrier mobility or

65   enhanced radiative recombination[14,15]. These open up new possibilities for photonic and

66   optoelectronic devices[15,16]. Further optimisation of these novel QDiP systems requires an in-

67   depth understanding of the mechanisms of carrier transport through them. It is unclear whether

68   the electronic coupling strength is sufficient to overcome disorder and generate electronic

69   bands, and how the fluctuating energy landscape influences the transport mechanism.

70

71   Recent advances have been made towards understanding exciton and charge dynamics

72   via optical techniques. Unlike device-level electrical methods that rely on charge injection to

73   fill shallow traps, optical techniques provide direct contactless means to fully account for the

74   influence of defects and polydispersity on transport. The charge transfer in halide-passivated

75   PbS CQDs has been studied via a donor-acceptor method using transient absorption

76   spectroscopy, demonstrating a spatially averaged mobility below 0.1 cm^2 V^{-1} s^{-1} and an inter-

77   dot hopping time of ~ 8 ps for 3.2 nm dots (ref.[17]). Time-resolved photoluminescence (PL)

78   microscopy measurement has been applied to probe exciton transport in CQD solids on

79   nanosecond timescales and reveal the exciton hopping mechanism with a time-dependent

80   diffusivity due to downhill energy migration[18]. These methods, however, cannot visualise the

81   ultrafast spatial dynamics due to the lack of suitable combinations of spatial precision and

82   temporal resolution. Thus, the non-equilibrium dynamics of CQD and QDiP solids remains

83   unexamined.

84

85   Here we report a direct visualisation of carrier transport in CQD and QDiP solids using

86   ultrafast transient absorption microscopy (TAM) with 10 fs temporal resolution and 10 nm

87   spatial precision (Figure 1a), and reveal a multi-stage transport mechanism. At early times

88   following photoexcitation band-like transport was observed to correlate with inter-particle

89   spacing and the degree of energetic disorder, resulting in significant diffusivities of up to 106

90    $cm^2 \ s^{-1}$. Over tens of picoseconds, an Auger-assisted transport for hot carriers takes place,

91   which is then followed by a slower sub-diffusive transport for thermally relaxed carriers. These

92   insights suggest a direct route to optimise the design of heterostructures and improve the

93   performance of CQD-based optoelectronics.

94

95   We focused our investigation on the ultrafast spatio-temporal dynamics of densely

96   packed CQD solids and the recently introduced QDiP system (Figure 1b). The PbS quantum

97   dots were synthesised and pre-exchanged with halide ligands as reported previously and the

98   size of CQDs tuned to yield an exciton peak at ~905 nm in films (see Methods)[14]. The

99   perovskite matrix consists of $CsPbBr_2I$, where the bromide and iodide ratio has been optimised

100   to achieve an ideal lattice matching with embedded PbS CQDs (Supplementary Fig.1),

101   resulting in epitaxially-aligned interfaces and excellent passivation.

102

103   By tuning the concentration of perovskite, we are able to tailor the average dot-to-dot

104   separation length (Figure 2a). The ground-state absorption spectra for QDiP heterostructures

105   show clear signatures corresponding to each constituent (Figure 2b). Without the introduction

106   of perovskite matrix, halide-capped PbS CQDs form randomly-packed ensembles with a high

107   packing density of ~64% (ref.[19]) and a tiny inter-dot separation ($l = 2 - 4$ Å)[20]. The exciton

108   absorption peak of CQD film is red-shifted by 91 meV compared with that of colloidal solution,

109   indicating the partial relaxation of quantum confinement due to strong electronic coupling

110   among dots. At low perovskite concentration (< 36% volume percentage), the matrix fills in

111   the voids among CQDs without noticeably separating the dots, evidenced by a negligible shift

112   of the exciton peak. As the perovskite ratio increases, larger inter-dot spacing is achieved,

113   resulting in reduced electronic coupling and, therefore, a blue-shift of PbS exciton absorption

114   peak in comparison to pure CQD films.

115

116   The two-dimensional transient absorption maps of QDiP heterostructures show the

117   ground-state bleach (GSB) bands of perovskite and CQDs – centred at 565 nm and 905 nm,

118   respectively – as well as a broad photoinduced absorption (PIA) band centred at 670 nm, which

119   is assigned to the intraband transitions of excited electrons or holes in CQDs – in particular the

120   transitions associated with 1P states[21,22] (Figure 2c, Supplementary Fig. 2). We emphasise

121   specific observations that are important for the interpretation of time-resolved microscopy

122   measurements. Upon photoexcitation above the bandgap of perovskite, carriers are generated

123   in both constituents. Within a few picoseconds excited carriers inject from the perovskite to

124   CQDs, as evidenced by the observation of identical time constants between the decay of GSB

125   band of perovskite and the rise of GSB band of CQDs (Figure 2c, Supplementary Fig. 3). On

126   the other hand, the corresponding rise components are absent in the kinetic profile for the PIA

127   band at 670 nm, indicating clearly that the observed PIA band is insensitive to the injected

128   carriers. This enables us to track, by probing at the PIA band, the motion of carriers that are

129   solely generated within and transport through CQDs, ruling out the carrier movement taking

130   place in perovskite.

131

132   Besides, the excited carriers in CQDs move energetically downhill to the lowest-energy

133   sites, resulting in a red-shift of the CQD bleach peak. The width of shift is determined by the

134   degree of energetic disorder – which can be quantified by the width of inhomogeneous

135   broadening of site energy, σ_{inh} – and the available thermal activation in the system, given by

136   the equation $\Delta E = -\frac{\sigma_{inh}^2}{2k_BT}$, where ΔE represents the energy difference before and after

137   thermalisation, k_B is the Boltzmann constant, and T is temperature[6,23]. By comparing the

138   energy shifts for different samples, we reveal a decrease in inhomogeneous broadening as the

139   perovskite content increases (Figure 2d). This indicates that the incorporation of lattice-

140   matched perovskite allows for an improved energy landscape in CQDs.

141

142   We then directly visualised the spatial carrier dynamics of QDiP heterostructures by

143   performing TAM measurements. We combined ultrafast transient absorption spectroscopy and

144   a high-performance optical microscope to deliver simultaneously extreme temporal resolution

145   (10 fs) and nanoscale localisation (Figure 1a)[24]. A near-diffraction-limited pump pulse, centred

146   at 580 nm (Supplementary Fig. 4), was used to excite the sample, generating a gaussian shaped

147   excited carrier distribution[25]. A time-delayed wide-field probe pulse was applied to spatially

148   resolve the transient response and therefore monitor the distribution of carrier population as a

149   function of time. These enabled us to track – by comparing the recorded images – the evolution

150   of photoinduced dynamics with sub-10 nm spatial precision, which is limited only by the

151   signal-to-noise characteristics of the system (see Methods)[26,27].

152

153   Pump fluence dependent measurements were carried out by varying excitation intensities,

154   with a minimum of $<N_{abs}>$ = 0.045 to maintain a signal-to-noise ratio. $<N_{abs}>$ is the average

155   number of photons absorbed per CQD[28], obtained from the product of the absorption cross-

156   section and the fluence per pulse[29,30]. By probing close to the PIA peak at 690 nm, we obtained

157   a series of TAM images that allow us to exclusively monitor the distribution of carriers

158   generated in CQDs. The TAM images were fitted with isotropic two-dimensional Gaussian

159   function as the initially generated carrier distribution closely resembles the diffraction-limited

160   pump and the spatial expansion occurs isotropically (Supplementary Figs. 5 and 6)[26,31]. This

161   enables us to extract the variance of carrier distribution at a certain time, σ_t^2, and quantify the

162   spatio-temporal evolution by calculating the mean-square-displacement, $\text{MSD} = \sigma_t^2 - \sigma_0^2$.

163

164   The time evolution of MSD obtained from halide-capped CQD solids clearly reveals

165   multiple distinct regimes for carrier transport (Figure 3a). Following photoexcitation, the

166   excited carriers are spatially distributed within the pump area, showing a σ_0 of 141 ± 10 nm

167   close to the diffraction limit of the microscope (133 nm, as shown in Supplementary Fig. 5).

168   Within a few hundreds of femtoseconds, the excited carriers undergo a pronounced spatial

169   expansion with a diffusion exponent (α) slightly larger than 1, indicative of an anomalous

170   diffusion as described by $\text{MSD} \propto t^\alpha \ (\alpha \neq 1),$ and a time-dependent diffusivity. After the initial

171   expansion (> 400 fs), the broadening of carrier distribution becomes progressively slower and

172   the MSD is observed to grow sub-linearly ($\alpha < 1$).

173

174   This later-time sub-linear growth of MSD is consistent with previous observations via

175   time-resolved PL microscopy[18] and indicates the sub-diffusive transport resulting from site-to-

176   site carrier hopping in CQD ensembles. The carriers migrate energetically downhill over the

177   disordered energy landscape, resulting in decreased hopping rates with time.

178

179   The early-time transport, however, has not been observed previously in CQD solids. We

180   calculated the diffusivity of carriers as $D(t) = \frac{MSD\,(t)}{2t}$ (ref.[18], Figure 3b) and extracted, for the

181   initial transport, a maximum diffusivity of 102 cm^2 s^{-1} at the lowest pump fluence. This

182 diffusivity corresponds to a carrier mobility of 3.94×10^3 cm^2 s^{-1} V^{-1} – which is about four

183 orders of magnitude higher than their mobility at equilibrium[17,32], and six times higher than

184 that of bulk PbS crystals at room temperature[33]. These observations suggest that the band-like

185 transport is accessed at the earliest times after photoexcitation of the strongly coupled CQD

186 solids. This regime – though persisting for only ~300 fs – allows carriers to propagate over a

187 significant distance of 80 nm, which corresponds to ~26 dots (Figure 3c). We note that, strictly

188 speaking, the extraction of diffusivity is not accurate for anomalous diffusion regimes, but

189 allows for a comparison with reported values in literature.

190

191   Fluence-dependent measurements further elucidate the effect of carrier density on

192 transport dynamics (Figure 3a, 3b). As $<N_{abs}>$ increases from 0.045 to 0.18, a higher

193 concentration of free carriers is generated, triggering Auger recombination (Supplementary Fig.

194 7)[34,35]. For the band-like regime, we observed that the diffusivity decreases at higher pump

195 fluence, suggesting that the carrier–carrier scattering limits the band-like transport. For the

196 following sub-diffusive transport, two different regimes are distinguished. On the timescale of

197 Auger recombination process (< 100 ps), MSD increases significantly with pump fluence (the

198 artificial broadening of σ is negligible up to 100 ps, Supplementary Fig. 8 and Supplementary

199 Note 1). We attribute this positive scaling of MSD with pump fluence to an Auger-assisted

200 carrier transport. Here, the Auger process generates energetic charge carriers with excess

201 kinetic energy, which assists in overcoming the potential barriers and energetic fluctuations,

202 and thus contributes to an increased hopping rate[36]. These carriers subsequently relax over tens

203 of picoseconds to reach thermal equilibrium with the lattice. When carriers are completely

204 cooled (>100 ps), a fluence-independent hopping regime takes over[37].

205

206   Previous studies have explored sub-diffusive transport in CQD solids and elucidated the

207   role of energetic disorder and inter-dot spacing in controlling the hopping process[18]. The band-

208   like transport process, however, has not been explicitly studied. To investigate the factors that

209   influence the distance of band-like transport, we performed TAM measurements for various

210   QDiP samples (Supplementary Figs. 6 and 9) and compared the temporal evolution of

211   diffusivity obtained at the lowest pump fluence (Figure 4a).

212

213   As the perovskite content increases, the inter-dot spacing and energy landscape change

214   correspondingly (Figure 2b and 2d). The initial diffusivity decreases remarkably as the inter-

215   dot separation increases, and the band-like regime is completely eliminated when CQDs are

216   well separated by perovskite (90 vol% perovskite). We attribute the slower initial propagation

217   to the reduced strength of electronic coupling and a lower degree of delocalisation. Intriguingly,

218   at perovskite loading of 40 vol% – the inter-dot separation and exciton peak position do not

219   change noticeably – a higher diffusivity is obtained ($D = 106$ cm^2 s^{-1}) compared to the pure

220   CQD solids (Figure 4c). We suggest that this effect may arise either due to enhanced dielectric

221   screening among dots[38] or improved structural uniformity of the film. These observations

222   support the strong correlation between the initial transport regime and the extent of electronic

223   coupling, which can be tuned by modifying the inter-particle spacing and matrix composition.

224

225   We also observed that the onset of the sub-diffusive regime is delayed as the perovskite

226   percentage increases. The reciprocal persistence time of band-like regime, $1/\tau_{band-like}$,

227   follows the same trend as the inhomogeneous broadening width (Figure 4d). This suggests that

228   the energetic disorder tends to disrupt the band-like transport regime, as would be expected for

229   such a process[39], following which the system moves to a sub-diffusive regime mediated by

230   Auger-assisted or normal hopping processes.

231

232   Our results illustrate that in a disordered system with a limited extent of delocalisation,

233 band-like transport and hopping-type transport can occur sequentially. We observed a volcano

234 trend in the distance of band-like transport as a function of perovskite content (Figure 4b). At

235 40 vol% perovskite loading, the largest band-like transport length of ~90 nm is obtained, which

236 corresponds to ~30 dots on average.

237

238   In summary, we have demonstrated a multi-stage carrier transport mechanism in both

239 CQD and QDiP solids. We observed an initial band-like transport that strongly correlates with

240 the extent of carrier delocalisation and energetic disorder, followed by an Auger-assisted sub-

241 diffusive transport before the carriers reach thermal equilibrium with the lattice, and a final

242 hopping regime for the cooled carriers. By harnessing materials structure and uniformity, an

243 extended band-like regime is obtained, resulting in up to 90 nm transport distance on sub-400

244 fs timescales. These findings provide new insights into the ultrafast dynamics in CQD solids

245 and heterostructures and offer guidelines for future material optimisation and device

246 engineering.

Methods

Sample preparation

The synthesis of CQDs was carried out following the reported procedures, and the preparation of QDiP films has been described previously. In summary, a solution-phase ligand-exchange process was carried out for CQDs. Precursors (lead iodide 0.05 M, lead bromide 0.05 M, cesium iodide 0.1 M, ammonium acetate (0.01 M) were mixed and dissolved in N,N-dimethylformamide (DMF). CQD solution in octane (5 mg/mL) was added to the precursor solution in a 1:1 volume ratio. These were mixed vigorously for 3 min until CQDs completely transferred to the DMF phase. The supernatant was removed and the DMF solution was then washed three times with octane. After the exchange process, CQDs were precipitated via the addition of toluene and then separated by centrifugation. This was followed by a drying process. The amount of perovskite matrix and dot-to-dot distance are tuned by the ratio of CQD to perovskite. For pure CQD films, butylamine was used as the solvent to disperse the dots. For QDiP solids, CQDs were redispersed in 0.4 M $CsPbBr_2I$ perovskite matrix solution in DMF and DMSO, and extra butylamine was added to improve the solubility of dots. The hybrid ink was deposited on glasses by spin-coating at 2000 rpm for 60 s to achieve an optimised thickness. This was followed by a mild annealing process ($100^{\circ}C$ for 10 min) to crystallise the matrix and remove solvent residues. Samples were encapsulated to avoid oxidation and degradation during measurements.

Transient absorption spectroscopy

Transient absorption spectra were recorded over short (200 fs – 2 ns) time delay using a femtosecond pump-probe setup. A light conversion PHAROS laser system with 400 µJ per pulse at 1030 nm with a repetition rate of 38 kHz was used. The output was divided into two parts: 1) one part was modified using a 4 mm YAG substrate to produce the continuum probe

272   beam from 520 to 950 nm; 2) another part was led into a narrow band optical parametric

273   oscillator system (ORPHEUS-LYRA, light conversion) to generate pump beam at 530 nm. The

274   probe pulse was delayed with a mechanical delay-stage (Newport), and a mechanical chopper

275   (Thorlabs) was used to generate on-off pump-probe pulse series. The areas of the pump and

276   the probe beam on the samples were 0.0625 mm^2 and 0.015 mm^2, respectively. A silicon line

277   scan camera (JAI SW-2000M-CL-80) with a visible spectrograph (Andor Solis, Shamrock)

278   was used to record the transmitted probe light.

279

280   Transient absorption microscopy

281   A Yb:KGW laser system (Pharos, Light Conversion) was used to provide 200 fs, 30 µJ pulses

282   at 1030 nm with 200 kHz repetition rate. The fundamental beam was divided by a beam splitter

283   and seeded two broadband white light continuum (WLC) stages. The probe WLC was

284   generated with a 3 mm YAG crystal and adjusted to cover the wavelength range from 650-950

285   nm by a fused-silica prism-based spectral filter. The pump WLC was generated with a 3 mm

286   sapphire crystal to achieve bluer WLC to 500 nm. The red-edge of pump beam is selected by

287   650 nm short-pass filter (Thorlabs, FESH650). A set of chirped mirrors (pump; 109811,

288   Layertec, probe; DCM9, Venteon) and a pair of fused silica wedges (Layertec) compressed the

289   pulses to 9.2 fs (pump) and 6.8fs (probe), as verified by second-harmonic generation

290   frequency-resolved optical gating (SHG-FROG) (see pulse characterisation in Supplementary

291   Fig. 4). The pump pulse was further pre-compressed with another set of chirped mirrors

292   (109811, Layertec) to compensate the dispersion in the microscope optics. The corresponding

293   cross-correlation curve simulated with the retrieved pump and probe temporal profiles given

294   in Supplementary Fig. 4 reveals an effective time resolution of 13 fs. Mechanical translation

295   stages (Newport, CONEX-AG-LS25-27P and Newport, M-ILS100HA) were used to delay the

296   probe with respect to the pump. A clean TEM00 mode for pump was achieved with a pinhole

297 and was collimated to completely fill the aperture of objective lens. The pump beam was then

298 focused onto the sample by an oil immersion objective (100x, effective NA of 1.1) to the near

299 diffraction limited spot (ca. 263 nm (FWHM) and 111 nm (width)) while the probe pulse was

300 delivered into the sample with the relatively large focal spot (ca. 15 μm) from the opposite

301 direction. The transmitted probe pulse was collected by the same objective and sent to an

302 EMCCD camera (QImaging, RoleraTM Thunder). The total magnification of the imaging

303 system was 288x. The scattered pump light was rejected by a 650 nm long-pass filter (Thorlabs,

304 FEL650) inserted in front of the camera. Differential imaging was achieved by modulating the

305 pump beam at 30 Hz by a mechanical chopper. The probing wavelengths were selected by

306 inserting a bandpass filter with 10 nm width. We note that the TAM images of each film were

307 obtained by averaging the images taken over 50 runs on at least five different spots across

308 multiple films, to eliminate artefacts from spot-to-spot variations.

309

Acknowledgements

315

Author Contributions

317 M.L., Y. S. and A. R. designed the study. M.L. and Y. S. contributed to all the experimental

318 work. S. D. V. carried out the transient absorption spectroscopy measurement. Z. Z.

319 synthesized the colloidal nanocrystals. A.R. supervised the project. M.L., Y. S. and A. R. wrote

320 the manuscript. All authors discussed the results and assisted in the preparation of the

321 manuscript.

References

1. Ekimov, A. I., Efros, Al. L. & Onushchenko, A. A. Quantum size effect in semiconductor microcrystals. *Solid State Commun.* **56**, 921–924 (1985).

2. Brus, L. E. Electron–electron and electron-hole interactions in small semiconductor crystallites: the size dependence of the lowest excited electronic state. *J. Chem. Phys.* **80**, 4403–4409 (1984).

3. Yazdani, N., Bozyigit, D., Yarema, O., Yarema, M. & Wood, V. Hole mobility in nanocrystal solids as a function of constituent nanocrystal size. *J. Phys. Chem. Lett.* **5**, 3522–3527 (2014).

4. Lee, J., *et al.* Band-like transport, high electron mobility and high photoconductivity in all-inorganic nanocrystal arrays. *Nat. Nanotech.* **6,** 348–352 (2011).

5. Choi, J.-H., *et al*. Bandlike transport in strongly coupled and doped quantum dot solids: a route to high-performance thin-film electronics. *Nano Lett.* **12**, 2631–2638 (2012).

6. Gilmore, R. H., Lee, E. M. Y., Weidman, M. C., Willard, A. P. & Tisdale, W. A. Charge carrier hopping dynamics in homogeneously broadened PbS quantum dot solids. *Nano Lett.* **17**, 893–901 (2017).

7. Liu, M., *et al.* Hybrid organic–inorganic inks flatten the energy landscape in colloidal quantum dot solids. *Nat. Mater.* **16,** 258–263 (2017).

347   8.   Nika, D. L., Pokatilov, E. P., Shao, Q. & Balandin, A. A. Charge-carrier states and light

348   absorption in ordered quantum dot superlattices. *Phys. Rev. B* **76**, 125417 (2007).

349   9.   Whitham, K., *et al.* Charge transport and localization in atomically coherent quantum

350   dot solids. *Nat. Mater.* **15,** 557–563 (2016).

351   10. Yang, J. & Wise, F. W. Effects of disorder on electronic properties of nanocrystal

352   assemblies. *J. Phys. Chem. C* **119**, 3338–3347 (2015).

353   11. Ning, Z. *et al.* Quantum-dot-in-perovskite solids. *Nature* **523**, 324–328 (2015).

354   12. Voznyy, O., Sutherland, B., Ip, A., Zhiotomirsky, D., Sargent, E. H. Engineering charge

355   transport by heterostructuring solution-processed semiconductors. *Nat. Rev.*

356   *Mater.* **2,** 17026 (2017).

357   13. Saidaminov, M. I. *et al*. Planar-integrated single-crystalline perovskite

358   photodetectors. *Nat. Commun.* **6**, 8724 (2015).

359   14. Liu, M., *et al.* Lattice anchoring stabilizes solution-processed semiconductors. *Nature*

360   **570,** 96–101 (2019).

361   15. Gong, X. *et al*. Highly efficient quantum dot near-infrared light-emitting diodes. *Nat.*

362   *Photonics* **10**, 253–257 (2016).

363   16. García de Arquer, *et al*. Field-emission from quantum-dot-in-perovskite solids. *Nat.*

364   *Commun.* **8,** 14757 (2017).

365   17. Proppe, A. H., *et al.* Picosecond charge transfer and long carrier diffusion lengths in

366   colloidal quantum dot solids. *Nano Lett.* **18**, 7052–7059 (2018).

367   18. AkseIrod, G. M., *et al.* Subdiffusive exciton transport in quantum dot solids. *Nano Lett*.

368   **14**, 3556−3562 (2014).

369   19. Choi, J.-H., *et al*. Bandlike transport in strongly coupled and doped quantum dot solids:

370   A route to high-performance thin-film electronics. *Nano Lett.* **12**, 2631−2638 (2012).

371   20. Lan, X., *et al.* Quantum dot solids showing state-resolved band-like transport. *Nat.*

372   *Mater.* **19,** 323–329 (2020).

373   21. Gesuele, F., *et al.* Ultrafast supercontinuum spectroscopy of carrier multiplication and

374   biexcitonic effects in excited states of PbS quantum dots. *Nano Lett.* **12**, 2658–2664

375   (2012).

376   22. EI-Ballouli, A. O., *et al*. Real-time observation of ultrafast intraband relaxation and

377   exciton multiplication in PbS quantum dots. *ACS Photonics* **1**, 285–292 (2014).

378   23. Bassler, H. Charge transport in disordered organic photoconductors – a Monte-Carlo

379   simulation study. *Phys. Stat. Sol. B* **175**, 15−56 (1993).

380   24. Von Diezmann, A., Shechtman, Y. & Moerner, W. E. Three-dimensional localization

381   of single molecules for super-resolution imaging and single-particle tracking. *Chem.*

382   *Rev.* **117**, 7244–7275 (2017).

383   25. Schnedermann, C. Ultrafast tracking of exciton and charge carrier transport in

384   optoelectronic materials on the nanometer scale. *J. Phys. Chem. Lett.* **10**, 6727–6733

385   (2019).

386   26. Sung, J., *et al.* Long-range ballistic propagation of carriers in methylammonium lead

387   iodide perovskite thin films. *Nat. Phys.* **16,** 171–176 (2020).

388   27. Schnedermann, C. *et al*. Sub-10 fs time-resolved vibronic optical microscopy. *J. Phys.*

389   *Chem. Lett.* **7**, 4854–4859 (2016).

390   28. Gao, J., Fidler, A. & Klimov, V. Carrier multiplication detected through transient

391   photocurrent in device-grade films of lead selenide quantum dots. *Nat.*

392   *Commun.* **6,** 8185 (2015).

393   29. Cademartiri. L., *et al*. Size-dependent extinction coefficients of PbS quantum dots. *J.*

394   *Am. Chem. Soc.* **128**, 10337-10346 (2006).

395   30. Moreels, I., *et al*. Size-dependent optical properties of colloidal PbS quantum dots. *ACS*

396   *Nano* **3**, 3023–3030 (2009).

397   31. Guo, Z., Manser, J. S., Wan, Y., Kamat, P. V. & Huang, L. Spatial and temporal

398   imaging of long-range charge transport in perovskite thin films by ultrafast

399   microscopy. *Nat. Commun.* **6**, 7471 (2015).

400   32. Sun, B., *et al*. Pseudohalide-exchanged quantum dot solids achieve record quantum

401   efficiency in infrared photovoltaics. *Adv. Mater*. **29**, 1700749 (2017).

402   33. Allgaier, R. S. Mobility of electrons and holes in PbS, PbSe, and PbTe between room

403   temperature and 4.2°K. *Phys. Rev.* **111**, 1029-1037 (1958).

404   34. Chen, T. *et al.* Metal–insulator transition in films of doped semiconductor

405   nanocrystals. *Nat. Mater.* **15**, 299 (2015).

406   35. Klimov, V. I. Optical nonlinearities and ultrafast carrier dynamics in semiconductor

407   nanocrystals. *J. Phys. Chem. B* **104**, 6112–6123 (2000).

408   36. Shabaev, A., Efros, A. L. & Efros, A. L. Dark and photo-conductivity in ordered array

409   of nanocrystals. *Nano Lett.* **13**, 5454–5461 (2013).

410   37. Gilmore, R. H., *et al*. Epitaxial dimers and Auger-assisted detrapping in PbS quantum

411   dot solids. *Matter* **5**, 1692–1694 (2019).

412   38. Hou, X., Kang, J., Qin, H. *et al.* Engineering Auger recombination in colloidal quantum

413   dots via dielectric screening. *Nat. Commun.* **10,** 1750 (2019).

414   39. Moix, J., Khasin, M. & Cao, J. Coherent quantum transport in disordered systems: I.

415   The influence of dephasing on the transport properties and absorption spectra on one-

416   dimensional systems. *New J. Phys.* **15**, 085010 (2013).

417

418
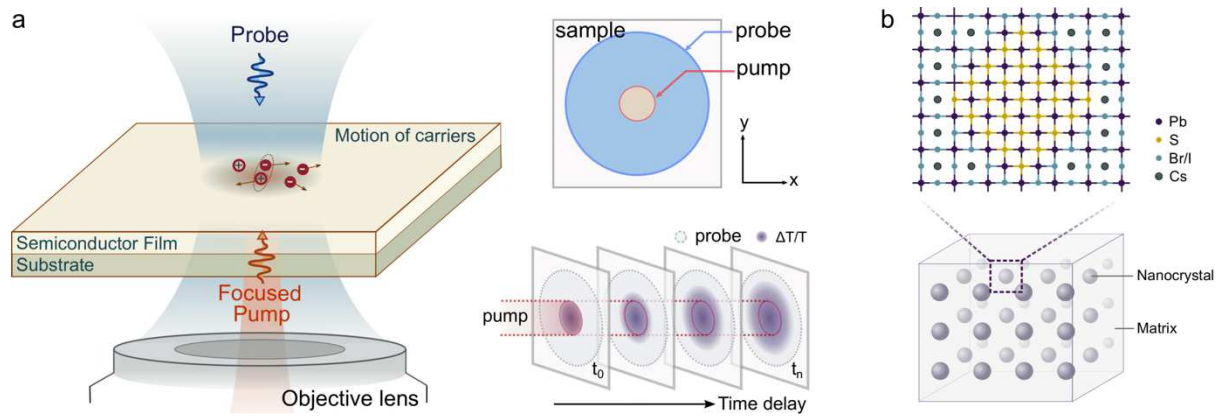
419

420 **Figure 1. Schematics of femtosecond transient absorption microscopy and QDiP solids. a,**

421 Schematics of TAM setup. A near-diffraction-limited (σ of 133 nm) and transform-limited

422 (9.2 fs, 580 nm) pump pulse is focused onto the sample through a high numerical aperture

423 microscope objective. A loosely focused (σ of 6.4 μm) probe pulse is focused from the top onto

424 the sample, and the transmitted probe is collected by the objective and imaged onto a digital

425 camera. Comparing the recorded spatial distribution of carrier population at different time

426 delays enables us to track the evolution of photoinduced dynamics with ~10 fs time resolution

427 and ~10 nm spatial precision, which is limited merely by the signal-to-noise characteristics of

428 the system. **b,** Schematic depiction of the atomistic model of a QDiP heterostructure. The

429 CsPbBr$_2$I matrix achieves an ideal lattice matching with embedded PbS CQDs, resulting in

430 epitaxially-aligned interfaces.

431

432
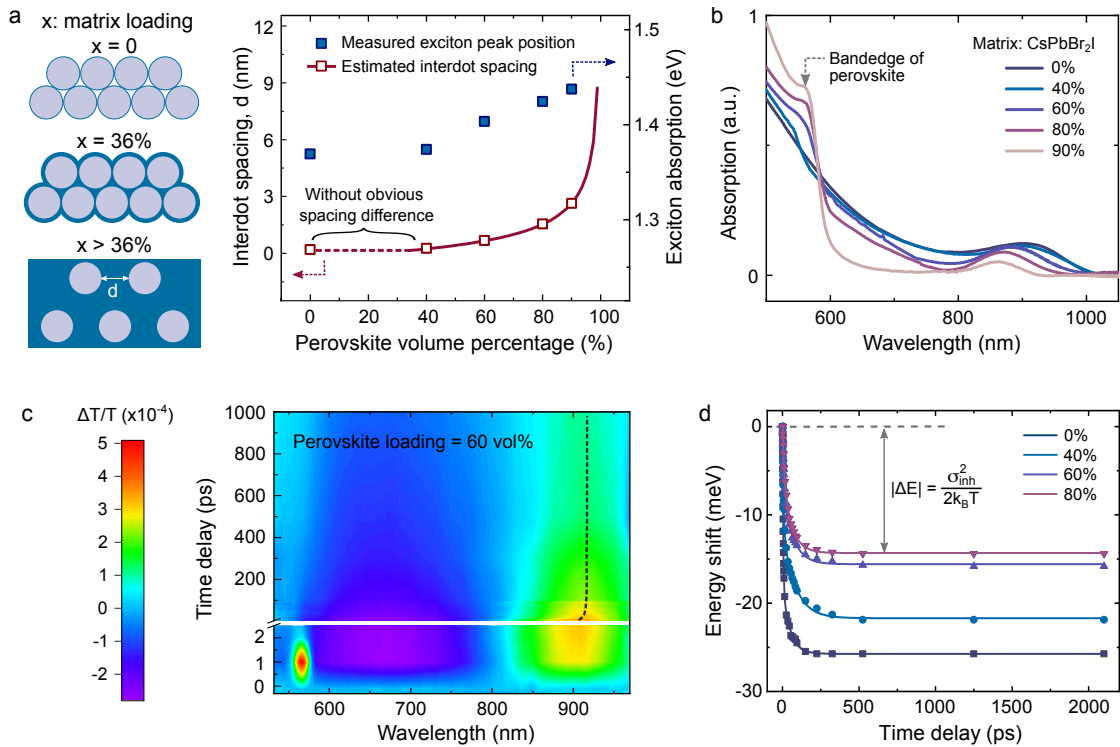
Figure 2. Structural and photophysical properties of CQD and QDiP solids. a, Inter-dot spacing (red open squares) and exciton absorption peak position (blue-filled squares) as a function of perovskite volume percentage. Without the introduction of perovskite, halide-capped PbS CQDs form randomly-packed ensembles with a high packing density (~64%) and a tiny inter-dot separation (2-4 Å). At low perovskite loadings (< 40 vol%), perovskites fill in the voids among CQDs without noticeably separating the dots. At high perovskite loadings (>40 vol%), increased inter-dot spacing results in a blue-shift of PbS exciton absorption peak. **b,** Matrix-tuned absorption spectra of CQD:perovskite heterostructures. **c,** Representative transient transmission map for QDiP solids (perovskite volume percentage is 60%). The positive regions centred at 565 nm and 900 nm correspond to the GSB bands of perovskite and CQDs, respectively. The negative region centred around 670 nm represents the broad photo-induced absorption band of CQDs. The black dashed line depicts the shift in the peak position of CQD transient bleach as a function of time. **d,** The shifts of CQD bleach peak energy over time for pure CQDs and QDiP heterostructures with various perovskite concentrations. The symbols represent the experimental values and the solid lines are fits to an exponential decay function. The red-shift of the CQD bleach peak demonstrates that photoexcited carriers funnel to the lower-energy sites in films. The final energy shift, ΔE, is determined by the energetic disorder and available thermal activation.

20
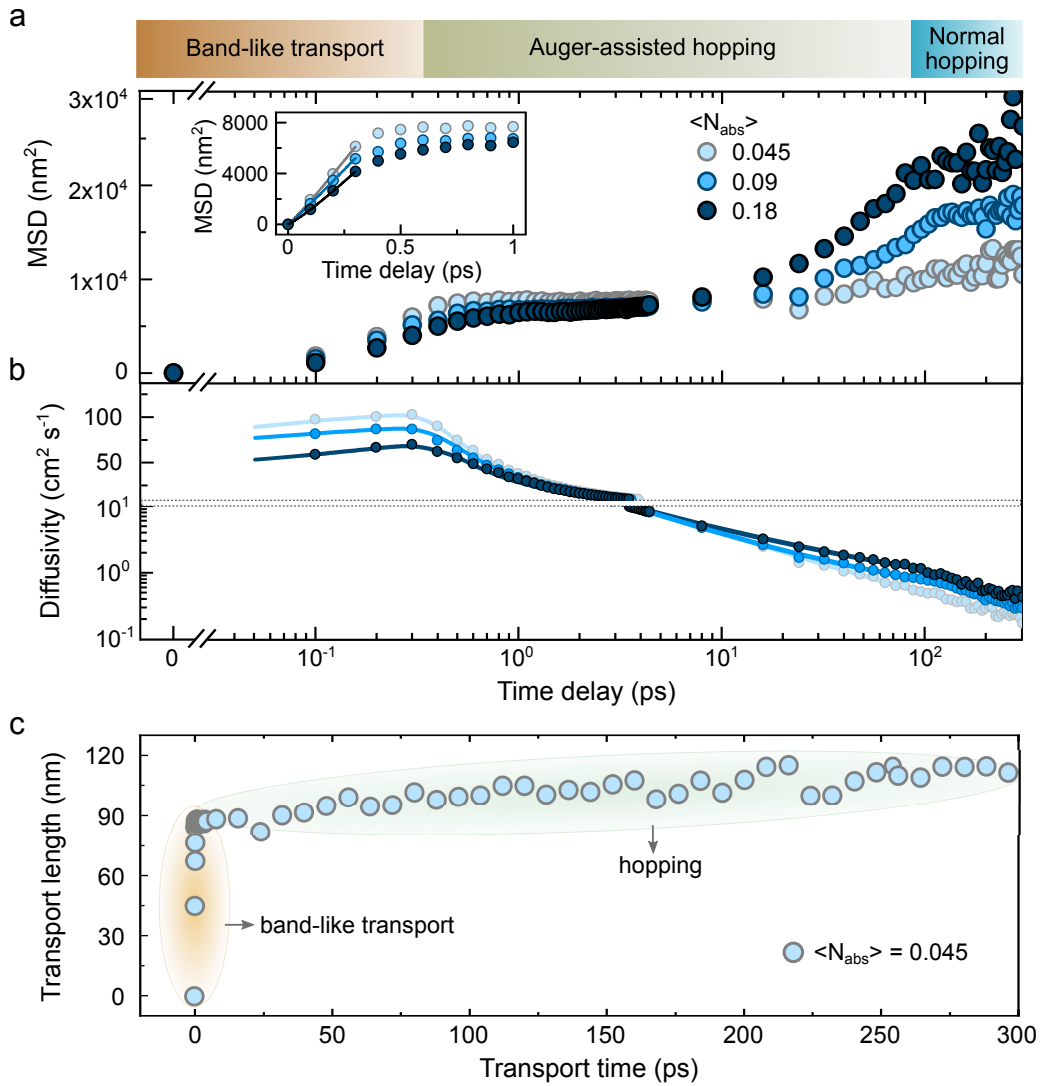
Figure 3. Dynamics of carrier propagation in pure CQD solids. a, Time evolution of MSD ($\sigma_t^2 - \sigma_0^2$) for pure CQD solids measured at different excitation intensities. $<N_{abs}>$ represents the average number of photons absorbed per CQD. The transport is divided into three regimes: band-like transport, Auger-assisted hopping, and thermally activated hopping. The inset figure shows a zoom-in view for the early time range (<1 ps), and fitted results are shown in solid lines to indicate a band-like transport during the initial hundreds of femtoseconds. **b,** Effective diffusivity as a function of time. Experimental values are displayed as symbols, while the fitted data are displayed as solid lines. **c,** Time evolution of carrier transport length, $\sqrt{\sigma_t^2 - \sigma_0^2}$, in CQD solids obtained at low pump fluence ($<N_{abs}> = 0.045$). Carriers rapidly migrate over ~80 nm within ~300 fs. The initial fast transport regime is followed by a much slower transport at longer time delays. This indicates a distinct transition from band-like transport to hopping-type transport.
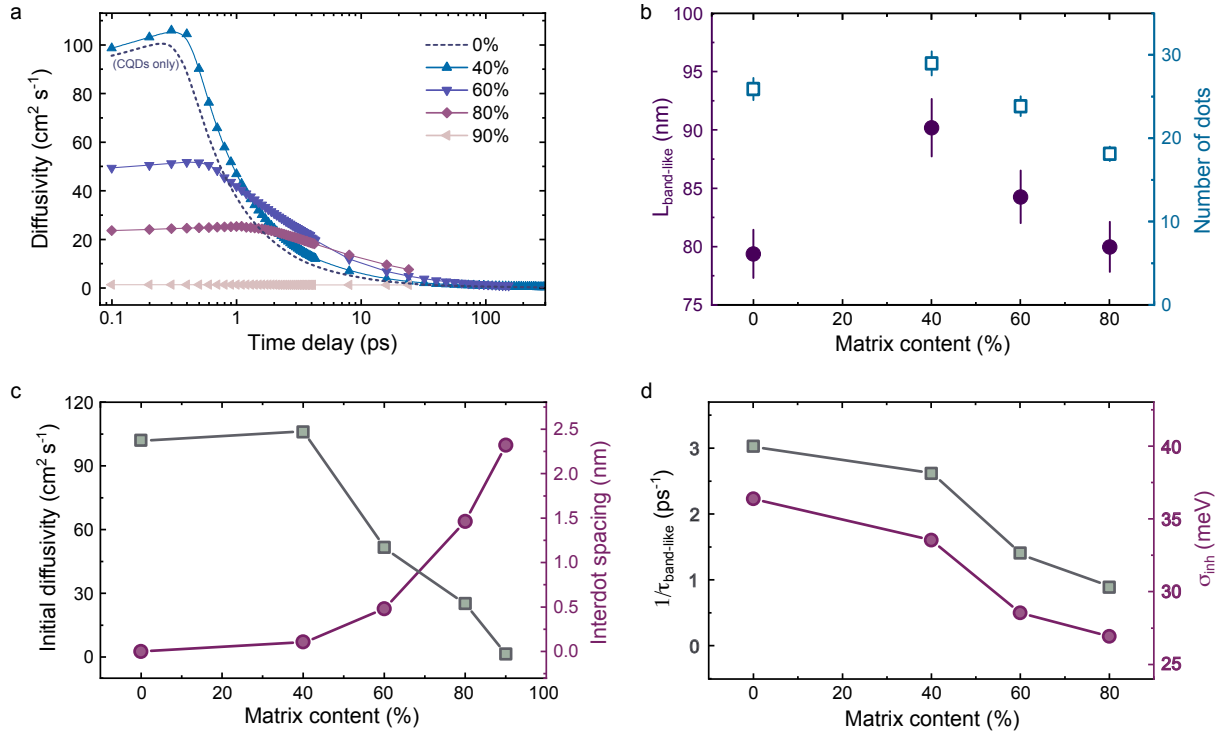
Figure 4. Carrier transport in QDiP solids at low pump fluence. a, Time evolution of diffusivity for QDiP heterostructures with various perovskite volume percentages. The dashed line represents the diffusivity for pure CQD control. **b,** Carrier transport length, $L_{band-like}$ ($\sqrt{\sigma_t^2 - \sigma_0^2}$), and the corresponding number of dots for the band-like transport region as a function of perovskite volume percentage. **c,** The maximum diffusivity and inter-dot spacing as a function of perovskite volume percentage. **d,** Reciprocal persistence time of band-like regime, $1/\tau_{band-like}$, and inhomogeneous broadening of site energy, σ_{inh}, as a function of perovskite volume percentage.
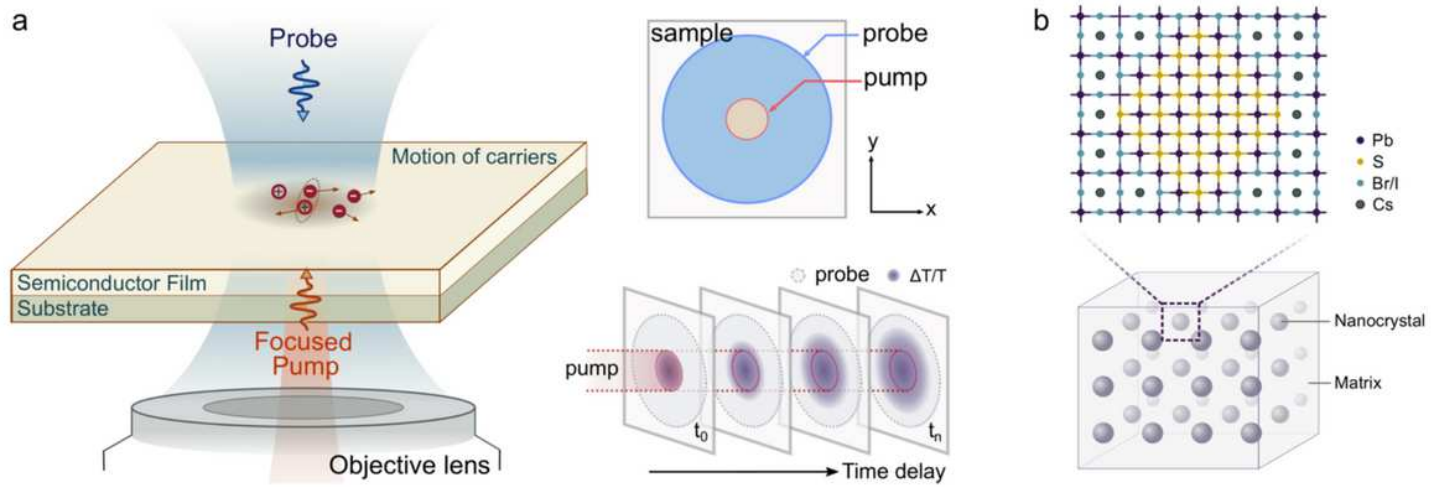
22

Figures

Figure 1

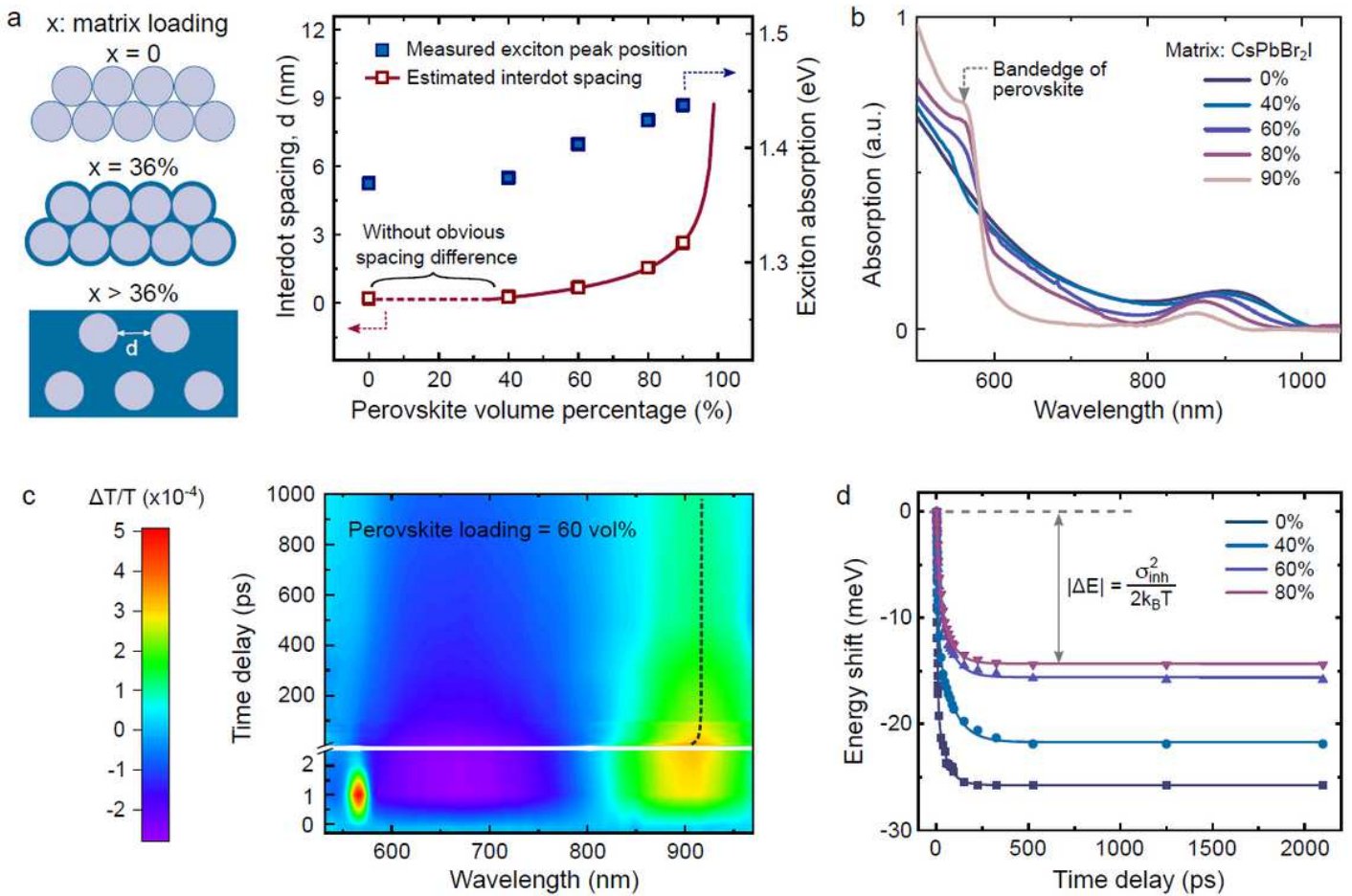Please see manuscript .pdf file for figure caption

Figure 2

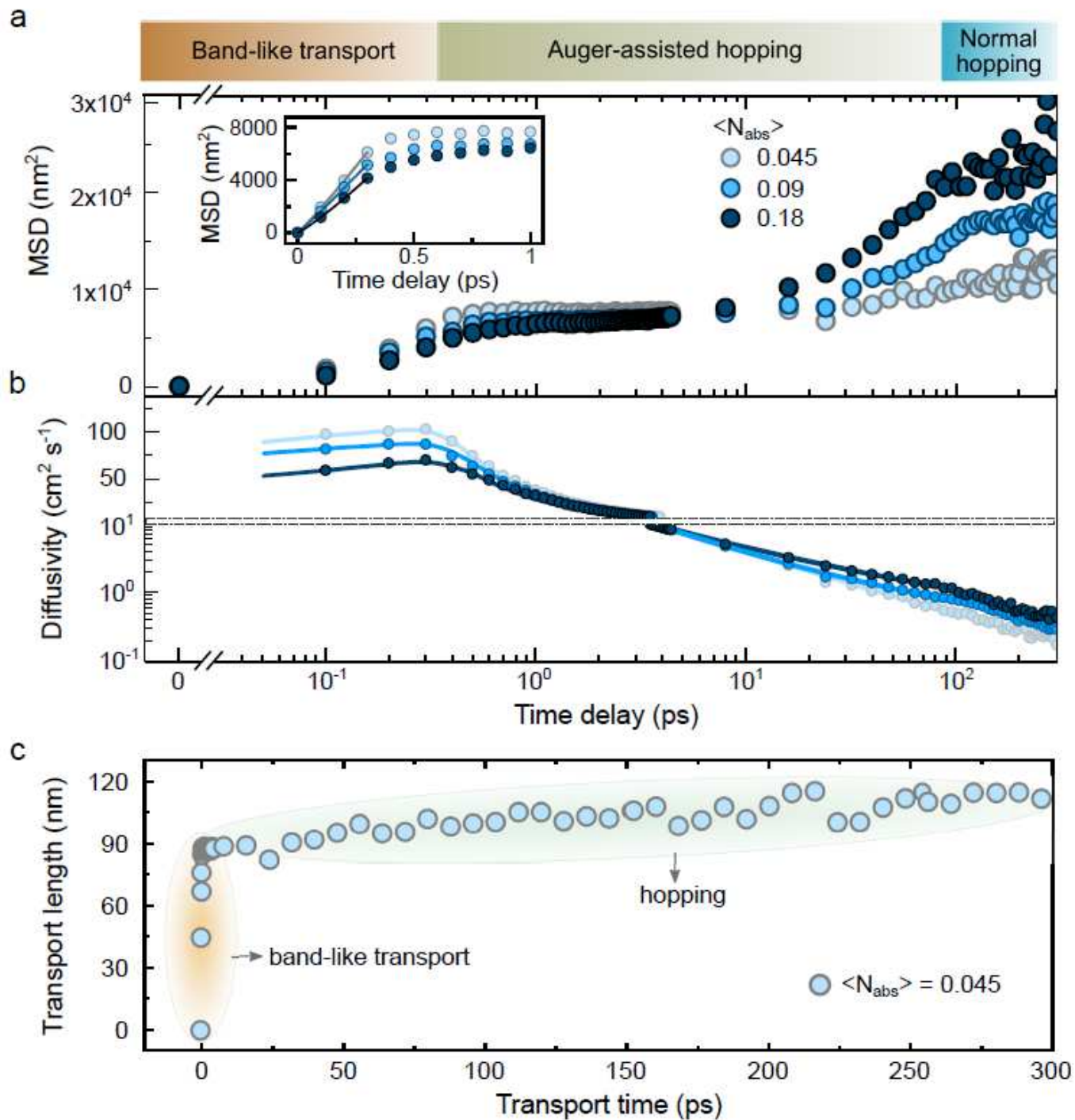Please see manuscript .pdf file for figure caption

Figure 3

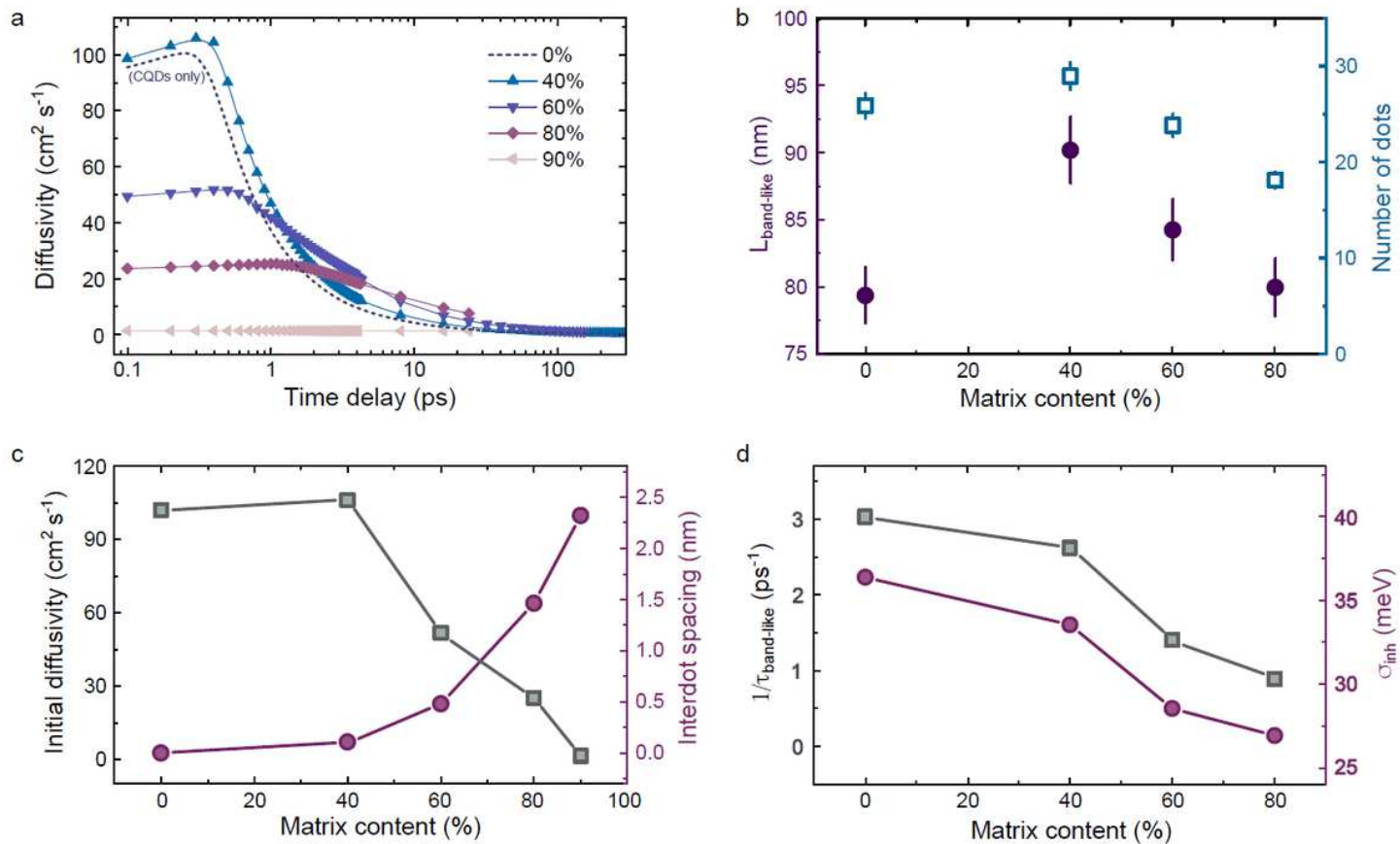Please see manuscript .pdf file for figure caption

Figure 4

Please see manuscript .pdf file for figure caption

Supplementary Files

This is a list of supplementary files associated with this preprint. Click to download.

- Supportinginformation.pdf